How to cite: *Angew. Chem. Int. Ed.* **2023,** *62,* e202212339
International Edition: doi.org/10.1002/anie.202212339
German Edition: doi.org/10.1002/ange.202212339

Organic Battery Cathodes

Anion Storage Chemistry of Organic Cathodes for High-Energy and High-Power Density Divalent Metal Batteries

*Yanlei Xiu, Anna Mauri, Sirshendu Dinda, Yohanes Pramudya, Ziming Ding, Thomas Diemant, Abhishek Sarkar, Liping Wang, Zhenyou Li, Wolfgang Wenzel, Maximilian Fichtner, and Zhirong Zhao-Karger**

Abstract: Multivalent batteries show promising prospects for next-generation sustainable energy storage applications. Herein, we report a polytriphenylamine (PTPAn) composite cathode capable of highly reversible storage of tetrakis(hexafluoroisopropyloxy) borate [B-(hfip)$_4$] anions in both Magnesium (Mg) and calcium (Ca) battery systems. Spectroscopic and computational studies reveal the redox reaction mechanism of the PTPAn cathode material. The Mg and Ca cells exhibit a cell voltage >3 V, a high-power density of $\sim\sim 3000$ W kg^{-1} and a high-energy density of $\sim\sim 300$ Wh kg^{-1}, respectively. Moreover, the combination of the PTPAn cathode with a calcium-tin (Ca–Sn) alloy anode could enable a long battery-life of 3000 cycles with a capacity retention of 60 %. The anion storage chemistry associated with dual-ion electrochemical concept demonstrates a new feasible pathway towards high-performance divalent ion batteries.

Introduction

Growing demand for electric vehicles and the implementation of intermittent renewable energies have stimulated the research interests in exploring sustainable, high-energy, high-power electrochemical storage systems.[1] Rechargeable Mg and Ca batteries are expected to provide efficient, safe, cost-effective battery solutions due to the merits of divalent working ions and metal anodes, which feature high-capacity, low tendency of dendrite formation and abundant natural resources.[2,3] However, the development of divalent-ion batteries is hindered by the absence of compatible electrolyte-cathode systems enabling reversible charge/discharge with high voltages.[3]

Given the high charge density of the Mg-ions (120 C mm^{-3} of Mg^{2+} vs. 54 C mm^{-3} of Li^+), intercalation of Mg-ion into an inorganic host is restricted by severe polarization and sluggish kinetics.[4] As a result, most of the conventional insertion metal oxide materials suffer from poor reversibility,[5] and only a few chalcogenides with soft anions and open structures allow reversible Mg-ion storage, such as Chevrel phase Mo_6S_8,[6] TiS_2,[7] MoS_2.[8] However, their low operating voltage (~ 1.1 V) and low energy density limit the potential for application. Different from inorganic ionic solids, organic materials offer more flexible ionic migration pathways due to the relatively weak intermolecular forces within organic compounds.[9] Additionally, charge storage of organic materials is based on the redox reaction of the functional groups, which is energetically more favorable for multivalent metal ions compared to the insertion-type inorganic materials.[9b,10] Moreover, the redox-active sites of the organic materials may allow multiple electron transfer per unit, hence providing the potential for high capacities at cell level.[10] In addition, featuring structural diversity, tunable properties, and environmental friendliness, organic electrode materials attract increasing attention for sustainable multivalent ion batteries.[11] Quinone-based cathodes with the redox mechanism of reversible enolation reactions have been studied in Mg and Ca battery systems, demonstrating improved cycling performance in comparison to most of the inorganic cathode counterparts.[11a,12,13] Nevertheless, the common n-type organic cathode materials generally exhibit a relatively low discharge voltage (<2 V), which is attributed to their intrinsically high energy level of the lowest unoccupied molecular orbital (LUMO) and relatively low reduction potentials.[14] Even if the voltage could be adjusted by molecular design,[15] it is still challenging to find n-type organic cathode materials offering a cell voltage beyond 3 V (vs. Mg/Mg^{2+}).[16]

[*] Y. Xiu, Dr. S. Dinda, Dr. T. Diemant, Dr. L. Wang, Dr. Z. Li, Prof. Dr. M. Fichtner, Dr. Z. Zhao-Karger
Helmholtz Institute Ulm (HIU) Electrochemical Energy Storage
Helmholtzstrasse 11, 89081 Ulm (Germany)
A. Mauri, Dr. Y. Pramudya, Z. Ding, Dr. A. Sarkar, Prof. Dr. W. Wenzel, Prof. Dr. M. Fichtner, Dr. Z. Zhao-Karger
Institute of Nanotechnology (INT), Karlsruhe Institute of Technology (KIT)
P.O. Box 3640, 76021 Karlsruhe (Germany)
E-mail: zhirong.zhao-karger@kit.edu
Z. Ding
Technical University of Darmstadt
64289 Darmstadt (Germany)

In contrast, organic materials based on anion storage chemistries and dual-ion working principles can potentially provide high voltages.[17] Polytriphenylamine (PTPAn) has been investigated in lithium (Li), sodium (Na) and potassium (K)-ion based electrochemical systems as a low-cost and scalable p-type organic cathode material.[18] However, the choice of suitable anodes is the limiting factor for these batteries, which diminishes the advantages of the cathodes with high potential and fast kinetics.[18] In contrast, coupling a PTPAn cathode with a feasible metallic anode, such as Mg and Ca, can combine the merits of both the cathode and anode in terms of energy density, cost and safety. The combination of a PTPAn cathode with an organic anode (i.e. perylene diimide-ethylene diamine) in magnesium perchlorate $Mg(ClO)_4$ electrolyte exhibited a rather low cell voltage (~1.1 V).[19] In fact, electrolytes with efficient ion and charge transport properties and sufficient stability play a crucial role in achieving high-energy batteries. In the past decades, substantial research efforts have been devoted to rational design of Mg and Ca electrolytes with high oxidative stability and efficient metal deposition.[20,3a] Recent progress made in the development of stable non-corrosive electrolytes provides new prospects for the realization of high-performance Mg and Ca batteries.[21,20c] In particular, magnesium tetrakis(hexafluoroisopropyloxy) borate ($Mg[B(hfip)_4]_2$) based electrolytes, possessing high oxidative stability (>4.3 V) and high ionic conductivity (~11 mS cm^{-1}), are suitable for exploring high-voltage cathodes.[22] Furthermore, the calcium analogue compound, calcium tetrakis(hexafluoroisopropyloxy)borate ($Ca[B(hfip)_4]_2$) enables reversible Ca stripping/plating at room temperature and shows suitable properties for improving Ca batteries.[23]

Herein, we demonstrate a dual-ion battery concept by integrating polythriphenylamine/graphene nanoplates (denoted as PTGNP) composite cathodes and $[B(hfip)_4]$-based electrolytes for high-voltage (>3 V) rechargeable Mg and Ca batteries. The dual-ion configuration can circumvent the issue of sluggish divalent-ion diffusion kinetics, enabling high electrochemical reversibility. For the first time, the reversible charge storage mechanism via the interaction of PTPAn with $[B(hfip)_4]^-$ anions was elucidated. Moreover, the evolution of resonance structures for redox-active PTPAn and its formed coordination complex were revealed by X-ray photoelectron spectroscopy (XPS), operando Raman spectroscopy, and density functional theory (DFT) calculations.

Results and Discussion

Polytriphenylamine (PTPAn) was synthesized by a one-step oxidation polymerization of triphenylamine (TPA) according to literature.[24,18a] Graphene nanoplates (GNPs) powder was used as electrical conductive substrate material for loading PTPAn. The PTGNP composite was fabricated through the reprecipitation of PTPAn in chloroform ($CHCl_3$) blended with the GNPs. (Figure 1a). The chemical structure of as-prepared PTGNP composite, PTPAn and the monomer TPA was characterized by the Fourier transform infrared spectra (FT-IR) (Figure S1), respectively. The characteristic IR vibration bands at 1585 cm^{-1}, 1487 cm^{-1} and 1315 cm^{-1} of the samples can be assigned to the C=C, C–C stretching and C–H bending vibration of phenyl rings in the TPA moiety, respectively. In addition, the strong signal at 1273 cm^{-1} refers to the C–N stretching vibration of the tertiary amine. The distinct bands at 813 cm^{-1} in the spectra of the PTPAn and PTGNP samples correspond to the C–H out-of-plane-bending of para-disubstituted benzene rings.[24,25,18b] Thus, the polymerization of the starting TPA monomers can be manifested. Besides, the intensity of the peak at 813 cm^{-1} was found to be lower for PTGNP composite than that for PTPAn, which might originate from the π–π interaction of redox-active PTPAn and graphene matrix, indicating an enhanced electronic conductivity for the PTGNP cathode. Furthermore, the NMR spectra of as-prepared PTPAn and TPA are also consistent with those as previously reported,[18b] verifying the successful preparation of the PTPAn cathode material (Figure S2).

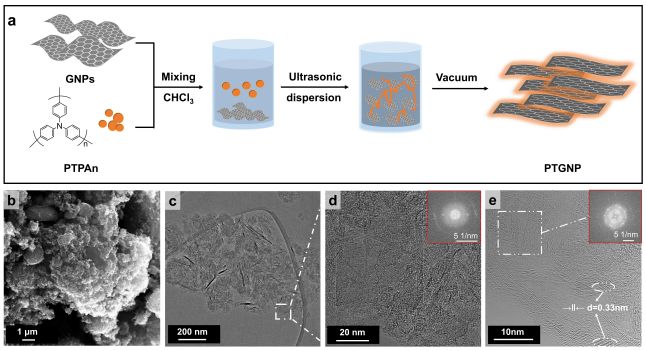

Figure 1. a) Scheme of the PTGNP composite fabrication procedure; Morphological features of the as-prepared PTGNP composite: b) SEM image, c–e) TEM images (insets show the FFT patterns extracted from HRTEM images).

The morphological structure of the as-prepared PTGNP composite was then analyzed by scanning electron microscopy (SEM) and transmission electron microscopy (TEM). As shown in Figure 1b and Figure S3, the composite particles consist of massive aggregates of primary PTGNP sheets in the size of ca. 30–200 nm. Plenty of agglomeration-derived pores (>50 nm) were observed, suggesting a macroporosity of the PTGNP composite, which is beneficial for the electrolyte penetration and charge-transfer in the cathode. After loading onto the GNP matrix, the particle size of the PTPAn polymer significantly decreased as presented by the TEM images (Figure S4a–f). Moreover, the entangled polymer composite particles could create some micro/mesoporous voids and largely maintain the surface area of the graphene nanoplates. TEM image in Figure 1c shows the homogeneity of the amorphous PTGNP composite particle. The graphitic and amorphous structure of the composite can be discerned in the high-resolution transmission electron microscopy (HRTEM) images and the corresponding Fast Fourier Transform (FFT) patterns (as shown in Figure 1d and Figure S4c,f). It indicates that the active PTPAn polymer was uniformly and intimately

attached to the carbon matrix, which ensures the sufficient electronic conductivity and high redox-active surface of the polymer cathode material (Figure 1e).

Further, the surface and porosity of the PTGNP composite was characterized by Brunauer–Emmett–Teller (BET) methods. The Nitrogen adsorption-desorption isotherms and pore size distribution plots are shown in Figure S5, respectively. The surface area of the composite was measured to be around 456 $m^2 g^{-1}$, which largely retains the surface area of the pristine GNP (750 $m^2 g^{-1}$), ensuring the fast ion diffusion within the active polymer electrode. In addition, the PTGNP composite possesses meso-porosity (5 to 45 nm), and micro-to-meso-porosity (1.7–5 nm). The large incremental volume of the mesopores could be beneficial to compensate the volume change of the cathodes upon the interaction with the anions, and hence enhancing the electrochemical reversibility.

To explore the electrochemical performance of the PTGNP cathode in Mg batteries, a dual-ion Mg||PTGNP full cell configuration was constructed as depicted in Figure 2a. Cyclic voltammetry (CV) was first carried out using a three-electrode cell with the PTGNP cathode as working electrode (WE) and polished Mg-foil as both counter electrode (CE) and reference electrode (RE) in 0.5 M $Mg[B(hfip)_4]_2$/DME electrolyte solution. As presented in Figure 2b, in the first anodic scan, one broad oxidation peak appeared at 3.2 V with a shoulder peak at 2.9 V, suggesting the insertion of $[B(hfip)_4]^-$ anions in the PTGNP cathode. In the following scans, these oxidation peaks shifted to 3.1 V and 2.8 V, respectively. The slight peak shift might be attributed to the improved kinetics related to the extended electrochemical active sites during cycling. In the cathodic scans, the corresponding reduction peaks located at 2.8 V and 2.5 V, respectively. These two pairs of redox peaks with reduced potential difference ~(~0.3 V) indicate highly reversible, fast charge-storage processes, which could be assigned to the redox reactions of the two isomeric PTPAn chemical structures.[18a]

Subsequently, the electrochemical properties of the PTGNP cathode were investigated by galvanostatic charge/discharge methods. Figure 2c shows typical voltage profiles of the Mg||PTGNP full cell at a current density of 545 mA g^{-1} (5C). In the first cycle, a major discharge plateau emerged in the range of 3.2 to 2.5 V, which shifted to 3.4–2.5 V in the following cycles. Simultaneously, the voltage hysteresis between the charge/discharge curves declined gradually. After the initial three cycles, the voltage profiles displayed nearly symmetrical characteristics. The main charge–discharge behavior and the derived differential capacity diagrams i.e. dQ/dV plots shown in Figure S6 were all in agreement with the CVs. Notably, an average operating voltage of ~3 V was realized with the combination of PTGNP cathode and Mg metal anode, surpassing those of previously reported cathode materials. Besides, a discharge capacity of 105 mAh g^{-1} could be delivered in the 10th cycle, which was almost 96 % of its theoretical value (109 mAh g^{-1}) corresponding to one-electron transfer per TPA unit, demonstrating a high energy density of 315 Wh kg^{-1}. It should be mentioned that the specific capacity and power

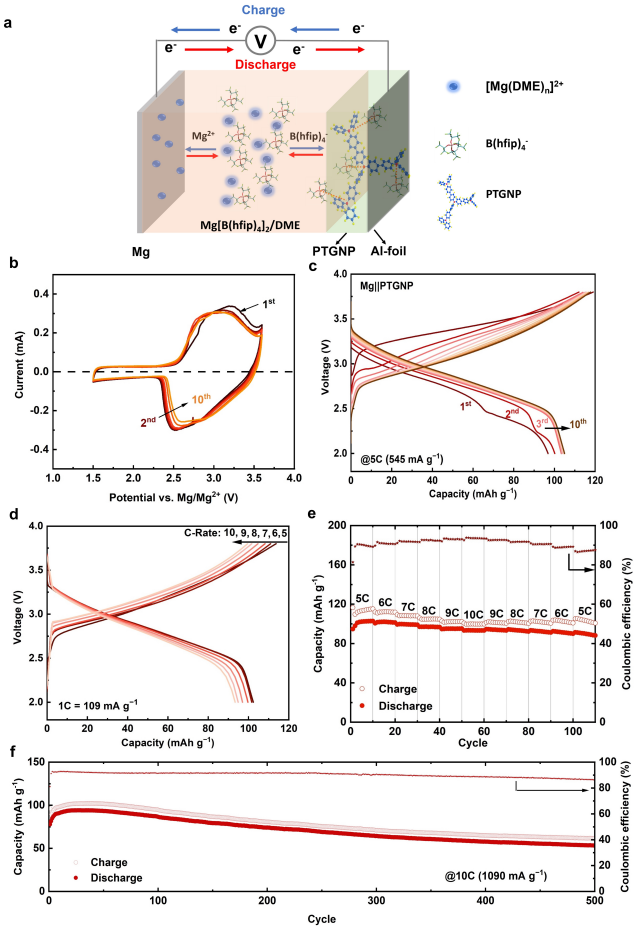

Figure 2. Electrochemical performance of the PTGNP cathode in Mg batteries with 0.5 M $Mg[B(hfip)_4]_2$/DME electrolyte. a) Scheme of the Mg||PTGNP dual-ion cell configuration and working principle; (b) CV curves of the PTGNP cathode vs. Mg_{RE} at a scan rate of 1 mV s^{-1}; c) galvanostatic voltage profiles of the composite cathode at 5C; d e) rate capability of PTGNP cathode at various C-rates (5 to 10C); f) cycling behavior of the Mg||PTGNP cell at 10C upon prolonged cycling. (1C = 109 mA g^{-1}).

density are based on the mass of the active cathode material in this work. The energy density of dual-ion systems at cell level could be generally limited by the requirement of a relatively large amount of electrolyte as both cation and anion act as charge carriers.[26,17b] Nevertheless, due to the two-electron transfer per divalent Mg/Ca cation and double mole ratio of the $[B(hfip)_4]_2$ anions of the conductive salt, the amount of electrolyte for the divalent dual-ion systems could be substantially reduced, leading to improved energy density compared to the monovalent ion counterparts. Besides, the natural abundance and feasibility of the divalent metal anodes (i.e., Mg and Ca) are particularly advantageous for cost-effective stationary energy storage applications.[27]

Further, the rate capability of PTGNP cathode was studied. As shown in Figure 2d, the charge/discharge curves maintained almost the same shape with minor discharge capacity decay for increasing C-rate from 5 to 10C, reflecting a rapid electron and ion transport. Meanwhile, the Coulom-

bic efficiency (CE) also reached up to 92% at 10C (1090 mA g^{-1}) as shown in Figure 2e. Remarkably, a power density of 2820 W kg^{-1} was obtained from a capacity of 94 mAh g^{-1} at 10C, which outperforms the majority of cathode materials and is desired for high-power Mg energy storage systems.[28]

Considering the improved CE at a higher C-rate, the long-term cycling stability of the PTGNP cathode was tested at 1090 mA g^{-1} (10C), as presented in Figure 2f. After the first 20 cycles, the cell delivered a maximum discharge capacity of ~93 mAh g^{-1} and retained 53 mAh g^{-1} after 500 cycles, suggesting a capacity decay rate of 0.86% per cycle. Note that the conductive carbon (i.e., GNP) has a negligible capacity contribution in the PTGNP cathode as shown in Figure S7. The reason for capacity fading and reduced CE (lower than 90% after 300 cycles) will be further investigated in the follow-up studies.

Further, we also explored the feasibility of the dual-ion battery concept for Ca systems. The Ca||PTGNP cell was assembled with a Ca-metal anode, PTGNP cathode and 0.25 M $Ca[B(hfip)_4]_2$/DME electrolyte. In galvanostatic cycling of these cells, the charge–discharge voltage profiles at a current density of 1090 mA g^{-1} (10C) showed a similar behaviour to what was observed in the Mg||PTGNP system (Figure 3a). In the first cycle, the discharge plateau exhibited in the range from 3.5 to 3.1 V, but gradually shifted to 3.7–3.2 V in the following four cycles, implying an average operating voltage of around 3.5 V. To the best of our knowledge, this is the highest cell voltage among the cathode materials for Ca batteries reported up to date. The increasing discharge voltage and capacity might be ascribed to the freshly deposited Ca on the anode, which also partially eliminated the voltage drop in the initial cycle.[29] Subsequently, a discharge capacity of 85 mAh g^{-1} was delivered at the 5th cycle, leading to an energy density of ~300 Wh kg^{-1} and a power density of 3000 W kg^{-1} (Figure 3c). However, the Ca-PTGNP system suffered from an inferior cyclic stability compared with the Mg system. The overpotential between the charge/discharge curves increased after 20 cycles followed by a severe capacity drop (Figure S8). As Ca–Sn alloys have been suggested as potential alternative anode for Ca-ion batteries,[12c] further experiments were conducted by integrating the PTGNP cathode with a $CaSn_3$-alloy anode. The half-cell comprised of the $CaSn_3$ anode and a Sn counter electrode exhibited favourable stability and compatibility with the borate electrolyte (Figure S9). Additionally, the CVs of PTGNP cathode coupled with $CaSn_3$ reference electrode represented similar electrochemical characteristics as the Mg system (Figure S10). Due to the relatively higher calcination/decalcination potential of the $CaSn_3$-alloy, the $CaSn_3$||PTGNP cell displayed a discharge plateau at a lower voltage range of 3.5 to 2.3 V, corresponding to an average working voltage of 2.8 V (Figure 3b). Remarkably, these cells could demonstrate an ultra-long cycle life, delivering a reversible capacity of ~50 mAh g^{-1} after 3000 cycles with capacity retention of around 60% of its initial value (86 mAh g^{-1}) as shown in Figure 3d. Moreover, the $CaSn_3$||PTGNP cell exhibited a higher CE compared with the Mg system due to the lower cut-off voltage at the charged state (3.6 V) that could alleviate the parasitic side reactions in the oxidation process.[30] It demonstrates that the PTGNP cathode can deliver high cycling stability and power capability with a high cell voltage for Ca batteries.

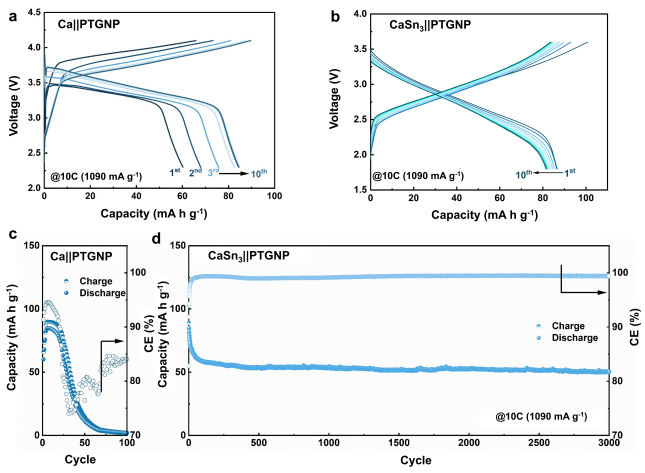

Figure 3. Electrochemical performance of the PTGNP cathode in Ca battery with 0.25 M $Ca[B(hfip)_4]_2$/DME electrolyte. Galvanostatic voltage profiles of the composite cathode at 10C with a) Ca-metal anode and b) $CaSn_3$-alloy anode; Cycling performance of c) Ca||PTGNP cell and d) $CaSn_3$||PTGNP cell at 10C (1C = 109 mA g^{-1}).

To elucidate the mechanism of the $[B(hfip)_4]^-$ anions storage in the PTGNP cathode, X-ray photoelectron spectroscopy (XPS) was employed to characterize the post-mortem PTGNP cathodes at various states during the initial charge–discharge process. In the survey spectra (Figure S11), three distinct peaks were observed: C1s (285 eV), O1s (533 eV) and F1s (688 eV). For the pristine electrode, the presence of O1s and F1s peak might be attributed to the residual C–O/C=O bonds of the graphene matrix and the CF_2 groups of the PTFE binder in the as-prepared cathode, respectively. In the fully charged state (3.8 V), the peak intensity of F1s increased largely, high-resolution detailed spectra in the F1s region are shown in Figure 4a. The new peak at 687.6 eV can be assigned to the C-F bond of $[B(hfip)_4]^-$ anions. In addition, an obvious signal related to the B–O bond (192.4 eV) was also identified in the B 1s spectra, indicating $[B(hfip)_4]^-$ anion insertion into the PTGNP cathode. When discharging to 2.0 V, both F1s and B1s peak intensity decreased again as $[B(hfip)_4]^-$ anions were extracted from the cathode. While no B1s signal could be detected in the discharged cathode, the F1s peak located at 687.6 eV was present most likely due to the high F content in the anion; however, its intensity was significantly lower compared to that in the charged state. These results indicate that most of the $[B(hfip)_4]^-$ anions could be removed from the cathode during discharging, while a small proportion decomposed. This could be one of the reasons for the relatively low CE in the initial cycles as shown in Figure 2e. Further, slightly increased CF_x concentrations in the discharged samples from the prolonged cycles could be confirmed as shown in Figure S12, Table S1. Moreover, the

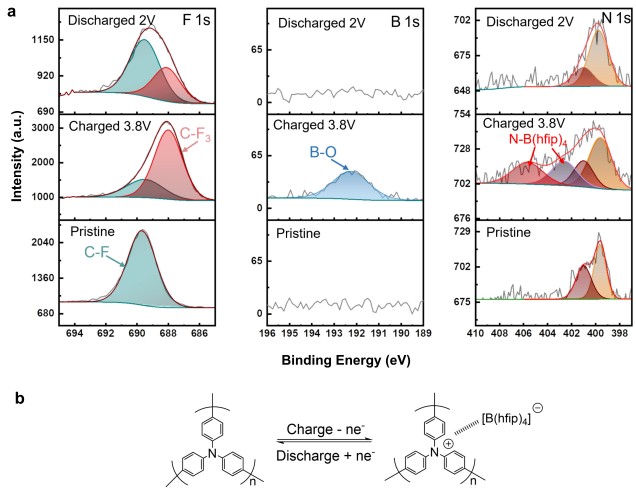

Figure 4. a) High-resolution XPS spectra of PTGNP cathodes in different states: F1s, B1s, N1s regions, b) Schematic illustration of $[B(hfip)_4]^-$ anion storage mechanism based on single-electron transfer of PTPAn.

reversible extraction of $[B(hfip)_4]^-$ anion could also be associated with the peak evolution of the redox-active N-center. The N1s spectra were broadened with the insertion of $[B(hfip)_4]^-$ anions and restored as the anions were released from the cathode. The original N1s spectrum can be resolved into two peaks located at 401.0 and 399.6 eV, stemming from the C–N bonds in the aforementioned PTPAn isomers (para or meta-substitution).[18a] For the charged cathode, the intensity of these N peaks decreased slightly, while two new peaks appeared at higher binding energy (i.e., 402.6 eV and 405.7 eV), implying that the neutral ion pair on the N-center was oxidized to positively charged radicals.[31] Simultaneously, these new peaks could be assigned to the formed N–$B(hfip)_4$ bond which resembles the coordination effect between PF_6^- anions and $PTPAn^+$ reported previously.[18c] Thus, the $[B(hfip)_4]^-$ anion storage mechanism can be verified as depicted in Figure 4b.

The Raman spectrum of pristine PTPAn is presented in the Supporting Information (Figure S13). The most characteristic Raman features can be outlined as follows: (i) two sharp and strongly overlapping bands, centered at 1600 cm^{-1} and 1610 cm^{-1} can be attributed to $\nu_{(C=C)}$ stretching vibration of an aromatic system; (ii) a band at 1286 cm^{-1} can be unambiguously assigned to $\nu_{(C-N)}$ stretching in an aromatic amine structure; (iii) a sharp band at 1170 cm^{-1} can be assigned to the $\nu_{(C-H)}$ in plane bending deformation in the aromatic ring; (iv) the 785 cm^{-1} band corresponds to the $\nu_{(C-H)}$ out of plane vibration. These observations match quite well with previous experimental and calculated results on polyaniline and polyaniline derivative materials.[32]

The redox reaction pathways of polyaniline derivatives transit through several topological forms containing radical cations at N-amine centers, which can be deduced through UV/Vis and Raman spectroscopy.[33] Consequently, in order to get a deeper insight into the essence of the electrochemical behavior of PTGNP cathodes, we have performed operando Raman measurements to scrutinize the structural evolution and redox mechanism of amine groups in PTPAn. Figure 5a depicts the charge/discharge profile of the Mg|| PTGNP cell in the first cycle, as well as an isoplot of the Raman scans at the PTGNP cathode. The contour plot shows the appearance and disappearance of several spectral features in the first charge cycle, which can be interpreted as the electrons extracted from the PTPAn. It fluctuates from aromatic to non-aromatic electronic configurations that shifts its electronic absorption maxima. Hence, the oxidized moiety sometimes shows resonance Raman and sometimes fall off from resonance Raman transition with respect to 532 nm excitation.

The spectral regions at 1600 cm^{-1} ($\upsilon_{(C=C)}$) and 1300 cm^{-1} ($\upsilon_{(C-N)}$) were deconvoluted to follow the radical formation and simultaneous $[B(hfip)_4]^-$ anion interaction processes during cycling. Figure 5b depicts deconvoluted Raman bands of $\upsilon_{(C-N)}$ during charge/discharge cycling. The deconvoluted Raman spectrum of the PTGNP cathode at the state of open circuit voltage (OCV) at 3.47 V shows an intense band at 1286 cm^{-1} ($\upsilon^{1286}_{(C-N)}$). Upon charging, the electrons are extracted from the nitrogen center, a band at 1315 cm^{-1} ($\upsilon^{1315}_{(C-N)}$) appears. At a higher voltage (from 3.68 V upwards), the band at $\upsilon^{1286}_{(C-N)}$ completely disappears and a new band at

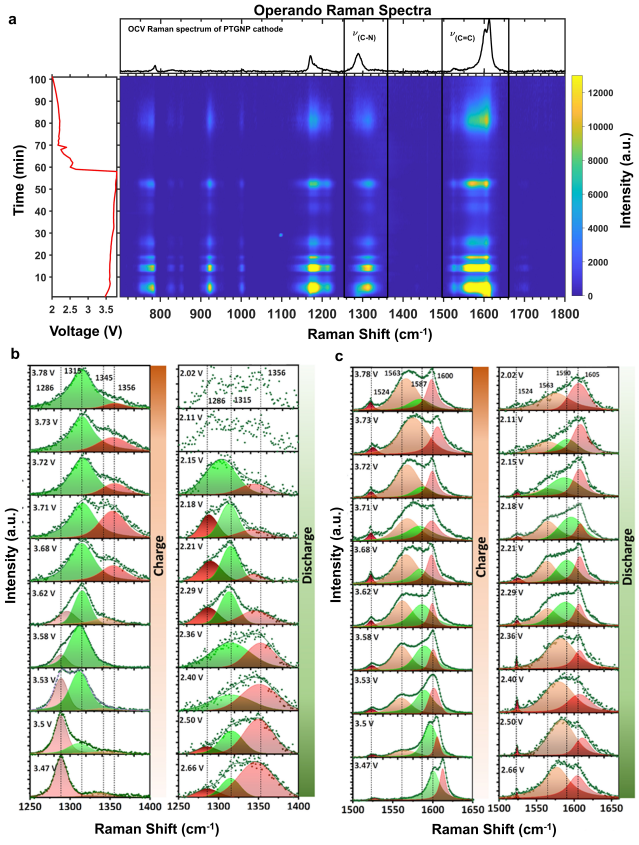

Figure 5. a) Isoplots of the operando Raman scans taken from the cathode side of the Mg|| PTGNP cell during the first charge/discharge cycle at 1C. Raman spectra in selected regions for the PTGNP cathode in the first charge/discharge cycle: b) 1250–1400 cm^{-1} ($\upsilon_{(C-N)}$), c) 1500–1650 cm^{-1} ($\upsilon_{(C=C)}$).

1356 cm^{-1} ($v^{1356}_{(C-N)}$) emerges. The intensity of the band $v^{1356}_{(C-N)}$ increases with respect to $v^{1315}_{(C-N)}$ and decreases at higher charging potentials (3.7 V upwards) again. Previous studies showed that the formation of oxidized polyaniline derivatives with cationic radical at the nitrogen center leads to a shift of $v_{(C-N)}$ from ~1280 cm^{-1} to ~1350 cm^{-1}.[33a,b] When this cationic radical is doped by an anionic counterpart of the electrolyte, the $v_{(C-N)}$ redshifts to a lower value at ~1320 cm^{-1}. In PTPAn, removal of one electron from amine (N1 in Figure S14) results in the formation of a cation radical which is immediately coordinated by a $[B(hfip)_4]^-$ anion, leading to the $v^{1286}_{(C-N)} \rightarrow v^{1315}_{(C-N)}$ shift in Raman measurements. The second electron is removed from the adjacent amine center (N2 in Figure S14), which leads to the formation of a bare cationic radical. However, the bulkiness of the $[B(hfip)_4]^-$ anion prevents the immediate doping, hence the increase in the intensity of $v^{1356}_{(C-N)}$. Instead, due to the charge repulsion and presence of conjugate amine segments, the radical cation shifts to N3 (N3 in Figure S14) to form a thermodynamically stable conformation and this center is then coordinated by a $[B(hfip)_4]^-$ anion which leads to reduction of the intensity of the $v^{1356}_{(C-N)}$ band. During the discharge scale, the opposite process is captured by the Raman spectroscopy analysis. Finally, at a lower discharge potential all the vibrational signatures are buried under a broad noisy band. This is probably due to the presence of excess electrons that shifts the wavelength of the resonance Raman process. During charge/discharge cycling, the cationic radical is also stabilized through delocalization by the formation of quinoid type structures. As shown in Figure 5c, the emergence of $v^{1563}_{(C=C)}$ and $v^{1587}_{(C=C)}$ band in the deconvoluted Raman spectra provides evidence for the formation of a significant amount of para-substituted quinone diamine type structures.[33b]

To further clarify the charge storage mechanism of the PTGNP cathode, density functional theory (DFT) calculations were carried out, in which the TPA unit was modelled as a molecule of PTPAn. As displayed in Figure 6a, both the highest occupied molecular orbital (HOMO) energy and the LUMO energy of PTPAn were significantly reduced in the charged state ($PTPAn^+$). In general, the HOMO energy level can be used to assess the electron donor ability. A reduced HOMO value means that further release of electrons from $PTPAn^+$ is energetically unfavourable, suggesting higher oxidation stability, while a lower LUMO energy level indicates a higher electron affinity. The resulting reduction of the LUMO-HOMO energy gap (1.68 eV) could effectively enhance the electronic conductivity of the redox-active polymer, promoting its interaction with charge carriers, and thus, facilitate fast reaction kinetics. Additionally, the redox potential in terms of single electron transfer and the formation energy of the $PTPAn^+$ -$[B(hfip)_4]^-$ coordination complex were also calculated as shown in Figure 6b. The cathode voltage obtained from DFT is 2.37 V ($\Delta E = 2.37$ eV). Based on the cohesive energy of metallic anodes (i.e., Mg, 1.51 eV and Ca, 1.84 eV),[34] the calculated full cell voltages are 3.13 V and 3.29 V for Mg and Ca systems, respectively,[35] which are in line with the average experimental discharge voltages, demonstrating a desirable high-voltage feature for divalent Mg and Ca batteries. Concurrently, the bulky nature of $[B(hfip)_4]^-$ anions could contribute to maintaining solid coordination structures at a higher operating voltage.[36] More information about the redox-active sites in PTPAn and the uptake of charge carriers can be obtained by calculation of electrostatic potential maps for PTPAn molecules in different charge states (Figure 6c). In the neutral state, excess electronic charge is mainly situated at the benzene rings (with red color) due to the π-conjugation and delocalization effects. After release of one electron, the positive charge (with blue color) was distributed unevenly in the molecule and mainly congregated around the N-atom, indicating it was the electroactive site with an electrophilic tendency. Meanwhile, the delocalization of electrons further strengthened, and an extended π-conjugation structure was formed around the N-radicals, which could effectively stabilize the positively charged molecule. During the charging process, $[B(hfip)_4]^-$ anions inserted and coordinated with $PTPAn^+$ for the charge balance. Due to steric effects, planar aromatic groups rotated slightly to better accommodate the charge carriers, which could change the vibrational mode of the final product and is in accordance with the results of the aforementioned operando Raman measurements.

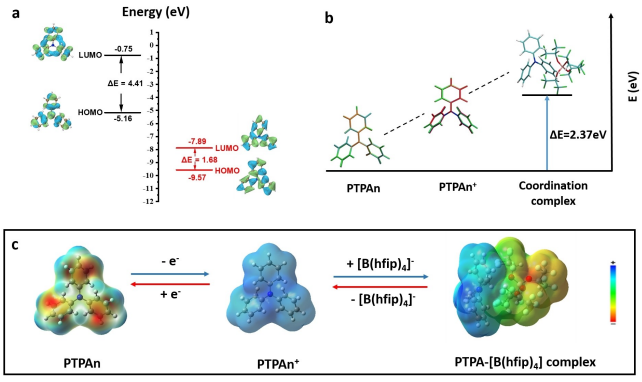

Figure 6. Density functional theory (DFT) calculations: a) Energy level diagram of pristine PTPAn (left) and $PTPAn^+$ (right); b) calculated three molecules and the corresponding formation energy changes, ΔE (charge distribution assigned as: 0 green, −1 orange, −2 cyan, +1 blue, and +2 red); c) electrostatic potential (ESP) maps of a PTPAn molecule and the formed coordination complex during charge storage process.

A more detailed investigation of the fast kinetics for charging/discharging the PTGNP cathodes was performed via CV measurements at different scan rates (Figure 7a). The redox reaction kinetics of the PTGNP cathode was analyzed according to Equation (1):

$$i = av^b \tag{1}$$

where i was the peak current, while a and b were the adjustable parameters to the scan rate v, respectively. As displayed in Figure 7b, the fitted b-values of anodic and cathodic scans were both higher than 0.9, suggesting a predominance of surface-controlled processes.[37] Quantifica-

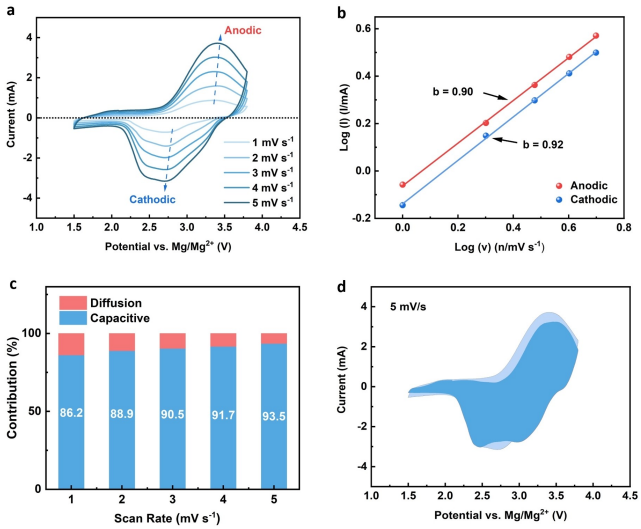

Figure 7. a) CV curves of the Mg||PTGNP cell at various scan rates from 1 to 5 mV s^{-1}; b) dependence of peak currents on scan rates; c) diffusion and surface-controlled capacity contribution at different scan rates; d) calculated surface-controlled (blue) and total current contribution (gray) of the PTGNP cathode at the scan rate of 5 mV s^{-1}.

tion of the surface-controlled and diffusion-controlled contribution was done using Equation (2):

$$i = k_1 v + k_2 v^{1/2} \quad (2)$$

where, k_1, k_2 were two constants, v was the scan rate, and $k_1 v$, $k_2 v^{1/2}$ represented the surface-controlled (pseudocapacitive) and diffusion-controlled portion, respectively.[37,38] It can be seen that the surface-controlled process hold significant current contributions (~85 %) at a low scan rate of 1 mV s^{-1} which even increased with rising scan rate (Figure 7c). Specifically, the contribution of the surface redox-activity was estimated to be approximately 93.5 % at a scan rate of 5 mV s^{-1} as illustrated in Figure 7d. It suggests that the rapid redox processes are facilitated by the high surface area and porous features of the PTGNP cathode by shortening the ion-migration pathways. Moreover, the weak-coordinating nature of the $[B(hfip)_4]^-$ anions offers high mobility of the anions within the electrolyte salt, boosting the migration of anionic charge carrier in the electrolyte and at the electrode interfaces, and consequently benefits to achieve fast kinetics.[36]

Conclusion

In summary, we have demonstrated a PTPAn composite cathode for high-voltage (>3 V) divalent Mg and Ca batteries based on $[B(hfip)_4]$ anion storage chemistry. Various spectroscopic analysis elucidates the reversible electrochemical redox reaction mechanism of the polymer cathode via the interaction of amine functional groups with the $[B(hfip)_4]$ anions. The computational analysis not only elaborated the charge storage mechanisms, but also revealed the narrow LUMO-HOMO energy gap of the PTPAn active material that is correlated the fast electrochemical kinetics of the organic cathodes. With a surface-controlled electrochemical process, the PTGNP cathodes could provide a high-power density of ~3000 W kg^{-1} and a high energy density ~300 Wh kg^{-1} for both rechargeable Mg and Ca batteries. Notably, the $CaSn_3$||PTGNP cells represent the state-of-the-art calcium-ion batteries in terms of the cell voltage (2.8 V), the long cycle-life (>3000 cycles) and capacity retention (60 %). The strategy of integrating the dual-ion cell configuration with the anion-storage mechanism provides a promising approach towards high-performance multivalent ion batteries.

Acknowledgements

We would like to acknowledge the European Union's Horizon 2020 research and innovation program under grant agreement No 824066 via the "E-MAGIC" project. This work contributes to the research performed at CELEST (Center for Electrochemical Energy Storage Ulm-Karlsruhe) and was partly funded by the German Research Foundation (DFG) under Project ID 390874152 (POLiS Cluster of Excellence). The authors acknowledge the support from the Karlsruhe Nano Facility (KNMF) for electron microscopy and spectroscopy. A.M. acknowledges the Deutsche Forschungsgemeinschaft (DFG, German Research Foundation) under Germany's Excellence Strategy for the Excellence Cluster "3D Matter Made to Order" (Grant No. EXC-2082/1-390761711) and the Carl Zeiss Foundation. Open Access funding enabled and organized by Projekt DEAL.

Conflict of Interest

The authors declare no conflict of interest.

Data Availability Statement

The data that support the findings of this study are available from the corresponding author upon reasonable request.

Keywords: Anion Storage Chemistry · Divalent Metal Ion Battery · Organic Cathode

[1] D. Larcher, J. M. Tarascon, *Nat. Chem.* **2015**, *7*, 19–29.
[2] a) R. Mohtadi, F. Mizuno, *Beilstein J. Nanotechnol.* **2014**, *5*, 1291–1311; b) Y. Tian, G. Zeng, A. Rutt, T. Shi, H. Kim, J. Wang, J. Koettgen, Y. Sun, B. Ouyang, T. Chen, et al., *Chem. Rev.* **2021**, *121*, 1623–1669.
[3] a) R. Mohtadi, O. Tutusaus, T. S. Arthur, Z. Zhao-Karger, M. Fichtner, *Joule* **2021**, *5*, 581–617; b) M. E. Arroyo-De Dompablo, A. Ponrouch, P. Johansson, M. R. Palacín, *Chem. Rev.* **2020**, *120*, 6331–6357.

[4] a) P. Canepa, G. Sai Gautam, D. C. Hannah, R. Malik, M. Liu, K. G. Gallagher, K. A. Persson, G. Ceder, *Chem. Rev.* **2017**, *117*, 4287–4341; b) V. V. Kulish, S. Manzhos, *RSC Adv.* **2017**, *7*, 18643–18649.
[5] a) S. Tepavcevic, Y. Liu, D. Zhou, B. Lai, J. Maser, X. Zuo, H. Chan, P. Král, C. S. Johnson, V. Stamenkovic, et al., *ACS Nano* **2015**, *9*, 8194–8205; b) J. S. Kim, W. S. Chang, R. H. Kim, D. Y. Kim, D. W. Han, K. H. Lee, S. S. Lee, S. G. Doo, *J. Power Sources* **2015**, *273*, 210–215.
[6] D. Aurbach, Z. Lu, A. Schechter, Y. Gofer, H. Gizbar, R. Turgeman, Y. Cohen, M. Moshkovich, E. Levi, *Nature* **2000**, *407*, 724–727.
[7] X. Sun, P. Bonnick, L. F. Nazar, *ACS Energy Lett.* **2016**, *1*, 297–301.
[8] Z. Li, X. Mu, Z. Zhao-Karger, T. Diemant, R. J. Behm, C. Kübel, M. Fichtner, *Nat. Commun.* **2018**, *9*, 5115.
[9] a) B. T. McAllister, L. T. Kyne, T. B. Schon, D. S. Seferos, *Joule* **2019**, *3*, 620–624; b) Z. Zhao-Karger, M. Fichtner, *Front. Chem.* **2019**, *6*, 656.
[10] Y. Liang, Y. Yao, *Joule* **2018**, *2*, 1690–1706.
[11] a) J. Xie, Q. Zhang, *Small* **2019**, *15*, 1805061; b) H. Ye, Y. Li, *Energy Fuels* **2021**, *35*, 7624–7636.
[12] a) H. Dong, O. Tutusaus, Y. Liang, Y. Zhang, Z. Lebens-Higgins, W. Yang, R. Mohtadi, Y. Yao, *Nat. Energy* **2020**, *5*, 1043–1050; b) Y. Xiu, Z. Li, V. Bhaghavathi Parambath, Z. Ding, L. Wang, A. Reupert, M. Fichtner, Z. Zhao-Karger, *Batteries Supercaps* **2021**, *4*, 1850–1857; c) Z. Zhao-Karger, Y. Xiu, Z. Li, A. Reupert, T. Smok, M. Fichtner, *Nat. Commun.* **2022**, *13*, 3849.
[13] a) B. Pan, D. Zhou, J. Huang, L. Zhang, A. K. Burrell, J. T. Vaughey, Z. Zhang, C. Liao, *J. Electrochem. Soc.* **2016**, *163*, A580–A583; b) W. Zhou, M. Zhang, X. Kong, W. Huang, Q. Zhang, *Adv. Sci.* **2021**, *8*, 2004490; c) B. Pan, J. Huang, Z. Feng, L. Zeng, M. He, L. Zhang, J. T. Vaughey, M. J. Bedzyk, P. Fenter, Z. Zhang, et al., *Adv. Energy Mater.* **2016**, *6*, 1600140; d) J. Bitenc, K. Pirnat, E. Žagar, A. Randon-Vitanova, R. Dominko, *J. Power Sources* **2019**, *430*, 90–94.
[14] a) Y. Ding, Y. Li, G. Yu, *Chem* **2016**, *1*, 790–801; b) Z. Song, H. Zhan, Y. Zhou, *Angew. Chem. Int. Ed.* **2010**, *49*, 8444–8448; *Angew. Chem.* **2010**, *122*, 8622–8626; c) S. Wang, L. Wang, Z. Zhu, Z. Hu, Q. Zhao, J. Chen, *Angew. Chem. Int. Ed.* **2014**, *53*, 5892–5896; *Angew. Chem.* **2014**, *126*, 6002–6006.
[15] J. Lüder, S. Manzhos, *Front. Chem.* **2020**, *8*, 83.
[16] N. A. Tran, N. Do Van Thanh, M. L. P. Le, *Chem. Eur. J.* **2021**, *27*, 9198–9217.
[17] a) Q. Liu, Y. Wang, X. Yang, D. Zhou, X. Wang, P. Jaumaux, F. Kang, B. Li, X. Ji, G. Wang, *Chem* **2021**, *7*, 1993–2021; b) T. Placke, A. Heckmann, R. Schmuch, P. Meister, K. Beltrop, M. Winter, *Joule* **2018**, *2*, 2528–2550.
[18] a) J. K. Feng, Y. L. Cao, X. P. Ai, H. X. Yang, *J. Power Sources* **2008**, *177*, 199–204; b) W. Ni, J. Cheng, X. Li, G. Gu, L. Huang, Q. Guan, D. Yuan, B. Wang, *RSC Adv.* **2015**, *5*, 9221–9227; c) L. Fan, Q. Liu, Z. Xu, B. Lu, *ACS Energy Lett.* **2017**, *2*, 1614–1620; d) W. Deng, X. Liang, X. Wu, J. Qian, Y. Cao, X. Ai, J. Feng, H. Yang, *Sci. Rep.* **2013**, *3*, 2671.
[19] D. Lu, H. Liu, T. Huang, Z. Xu, L. Ma, P. Yang, P. Qiang, F. Zhang, D. Wu, *J. Mater. Chem. A* **2018**, *6*, 17297–17302.
[20] a) R. Attias, M. Salama, B. Hirsch, Y. Goffer, D. Aurbach, *Joule* **2019**, *3*, 27–52; b) Q. Wei, L. Zhang, X. Sun, T. L. Liu, *Chem. Sci.* **2022**, *13*, 5797–5812; c) K. V. Nielson, J. Luo, T. L. Liu, *Batteries Supercaps* **2020**, *3*, 766–772.
[21] a) O. Tutusaus, R. Mohtadi, T. S. Arthur, F. Mizuno, E. G. Nelson, Y. V. Sevryugina, *Angew. Chem. Int. Ed.* **2015**, *54*, 7900–7904; *Angew. Chem.* **2015**, *127*, 8011–8015; b) Z. Zhao-Karger, M. E. Gil Bardaji, O. Fuhr, M. Fichtner, *J. Mater. Chem. A* **2017**, *5*, 10815–10820; c) J. Luo, Y. Bi, L. Zhang, X. Zhang, T. L. Liu, *Angew. Chem. Int. Ed.* **2019**, *58*, 6967–6971; *Angew. Chem.* **2019**, *131*, 7041–7045; d) J. T. Herb, C. A. Nist-Lund, C. B. Arnold, *ACS Energy Lett.* **2016**, *1*, 1227–1232.
[22] Z. Zhao-Karger, R. Liu, W. Dai, Z. Li, T. Diemant, B. P. Vinayan, C. Bonatto Minella, X. Yu, A. Manthiram, R. J. Behm, et al., *ACS Energy Lett.* **2018**, *3*, 2005–2013.
[23] Z. Li, O. Fuhr, M. Fichtner, Z. Zhao-Karger, *Energy Environ. Sci.* **2019**, *12*, 3496–3501.
[24] C. Takahashi, S. Moriya, N. Fugono, H. C. Lee, H. Sato, *Synth. Met.* **2002**, *129*, 123–128.
[25] C. Kvarnström, A. Petr, P. Damlin, T. Lindfors, A. Ivaska, L. Dunsch, *J. Solid State Electrochem.* **2002**, *6*, 505–512.
[26] Y. Sui, C. Liu, R. C. Masse, Z. G. Neale, M. Atif, M. AlSalhi, G. Cao, *Energy Storage Mater.* **2020**, *25*, 1–32.
[27] a) K. V. Kravchyk, P. Bhauriyal, L. Piveteau, C. P. Guntlin, B. Pathak, M. V. Kovalenko, *Nat. Commun.* **2018**, *9*, 4469; b) X. Lei, Y. Zheng, F. Zhang, Y. Wang, Y. Tang, *Energy Storage Mater.* **2020**, *30*, 34–41.
[28] A. B. Ikhe, J. Y. Seo, W. B. Park, J. W. Lee, K. S. Sohn, M. Pyo, *J. Power Sources* **2021**, *506*, 230261.
[29] J. Bitenc, A. Scafuri, K. Pirnat, M. Lozinšek, I. Jerman, J. Grdadolnik, B. Fraisse, R. Berthelot, L. Stievano, R. Dominko, *Batteries Supercaps* **2021**, *4*, 214–220.
[30] J. Xiao, Q. Li, Y. Bi, M. Cai, B. Dunn, T. Glossmann, J. Liu, T. Osaka, R. Sugiura, B. Wu, et al., *Nat. Energy* **2020**, *5*, 561–568.
[31] a) Y. Yamada, H. Tanaka, S. Kubo, S. Sato, *Carbon* **2021**, *185*, 342–367; b) B. Russ, M. J. Robb, B. C. Popere, E. E. Perry, C. K. Mai, S. L. Fronk, S. N. Patel, T. E. Mates, G. C. Bazan, J. J. Urban, et al., *Chem. Sci.* **2016**, *7*, 1914–1919.
[32] a) A. V. Szeghalmi, M. Erdmann, V. Engel, M. Schmitt, S. Amthor, V. Kriegisch, G. Nöll, R. Stahl, C. Lambert, D. Leusser, et al., *J. Am. Chem. Soc.* **2004**, *126*, 7834–7845; b) C. Su, F. Yang, L. Ji, L. Xu, C. Zhang, *J. Mater. Chem. A* **2014**, *2*, 20083–20088.
[33] a) V. F. Kalasinsky, T. S. Little, *J. Raman Spectrosc.* **1980**, *9*, 224–229; b) T. Cervantes, G. Louarn, H. De Santana, L. Skorka, I. Kulszewicz-Bajer, *J. Phys. Chem. B* **2015**, *119*, 1756–1767; c) Z. Morávková, I. Šedenková, P. Bober, *Appl. Sci.* **2020**, *10*, 2091.
[34] C. Kittel, *Introduction to Solid State Physics*, Wiley & Sons, New York, **2004**.
[35] M. Saubanère, M. Ben Yahia, S. Lebègue, M. L. Doublet, *Nat. Commun.* **2014**, *5*, 5559.
[36] P. Jankowski, Z. Li, Z. Zhao-Karger, T. Diemant, M. Fichtner, T. Vegge, J. M. G. Lastra, *Energy Storage Mater.* **2022**, *45*, 1133–1143.
[37] T. S. Mathis, N. Kurra, X. Wang, D. Pinto, P. Simon, Y. Gogotsi, *Adv. Energy Mater.* **2019**, *9*, 1902007.
[38] X. Yang, A. L. Rogach, *Adv. Energy Mater.* **2019**, *9*, 1900747.

Manuscript received: August 21, 2022
Accepted manuscript online: October 21, 2022
Version of record online: December 2, 2022